



HAL
open science

Constraining the mass distribution of galaxies using galaxy-galaxy lensing in clusters and in the field

Marceau Limousin, Jean Paul Kneib, Priyamvada Natarajan

► **To cite this version:**

Marceau Limousin, Jean Paul Kneib, Priyamvada Natarajan. Constraining the mass distribution of galaxies using galaxy-galaxy lensing in clusters and in the field. *Monthly Notices of the Royal Astronomical Society*, 2005, 356, pp.309. 10.1111/j.1365-2966.2004.08449.x . hal-00015141

HAL Id: hal-00015141

<https://hal.science/hal-00015141>

Submitted on 17 Jan 2021

HAL is a multi-disciplinary open access archive for the deposit and dissemination of scientific research documents, whether they are published or not. The documents may come from teaching and research institutions in France or abroad, or from public or private research centers.

L'archive ouverte pluridisciplinaire **HAL**, est destinée au dépôt et à la diffusion de documents scientifiques de niveau recherche, publiés ou non, émanant des établissements d'enseignement et de recherche français ou étrangers, des laboratoires publics ou privés.

Constraining the mass distribution of galaxies using galaxy–galaxy lensing in clusters and in the field

Marceau Limousin,¹* Jean-Paul Kneib^{1,2} and Priyamvada Natarajan³

¹*Observatoire Midi-Pyrénées, UMR5572, 14 Avenue Edouard Belin, 31400 Toulouse, France*

²*Caltech, Astronomy, MC105-24, Pasadena, CA 91125, USA*

³*Department of Astronomy, Yale University, PO Box 208101, New Haven, CT 06250, USA*

Accepted 2004 September 23. Received 2004 September 19; in original form 2004 June 2

ABSTRACT

We present a maximum-likelihood analysis of galaxy–galaxy lensing effects in galaxy clusters and in the field. The aim is to determine the accuracy and robustness of constraints that can be obtained on galaxy halo properties in both environments: the high-density cluster and the low-density field. This paper is theoretically motivated, therefore we work exclusively with simulated data (nevertheless defined to match observations) to study the accuracy with which input parameters for mass distributions for galaxies can be extracted. We model galaxies in the cluster and the field using a wide range of mass profiles: the truncated pseudo-isothermal elliptical mass distribution, the Navarro–Frenk–White profile, and a power-law model with a core radius. We find that independent of the choice of profile the mean mass of galaxies (of the order of $10^{12} M_{\odot}$) can be estimated to within 15 per cent from ground-based data and with an error of less than 10 per cent with space observations. Additionally, robust constraints can be obtained on the mean slope of the mass profile. The two standard parameters that characterize galaxy halo models, the central velocity dispersion and the truncation radius, can also be retrieved reliably from the maximum-likelihood analysis. We find that there is an optimal scale R_{\max} which marks the boundary between lenses that effectively contribute to the measured shear. Lenses beyond R_{\max} in fact dilute the shear signal. Furthermore, going beyond the usual formulation, we propose a reparametrization of the mass models that allows us to put yet stronger constraints on the aperture mass of a galaxy halo (with less than 10 per cent error). The gain in signal-to-noise using space observations, expected for instance with the proposed *SuperNova/Acceleration Probe (SNAP)* satellite compared to ground-based data in terms of accuracy of retrieving input parameters, is highly significant.

Key words: gravitational lensing – galaxies: general – galaxies: haloes – cosmology: miscellaneous – dark matter.

1 INTRODUCTION

Gravitational lensing has now become a popular tool to measure the mass distribution of structure in the Universe on a range of scales. Recently, there has been considerable progress in mapping the mass distribution on relatively large scales using cosmic shear (Refregier 2003), and on cluster scales combining strong and weak lensing features (Gavazzi et al. 2003; Kneib et al. 2003). On the scale of individual galaxies as well, there has been much work carried out on modelling and understanding multiple quasar systems (Fassnacht et al. 1999; Phillips et al. 2000). In fact, in many cases it has become clear that it is almost never a unique lens that is responsible for the detected lensing and the presence of a nearby galaxy, group or

cluster along the line of sight plays an important role in inducing the shear and amplification (Keeton, Kochanek & Seljak 1997; Kneib, Cohen & Hjorth 2000; Möller et al. 2002). In other words, there are likely no clean lines of sight and comprehensive modelling is needed to map the lensing configuration accurately. Therefore, the mass mapping problem is best tackled using an ‘inverse’ approach where the adopted method is to model the distribution of matter around many lines of sight, and to optimize the mass distribution to match the observations as closely as possible.

Analysing galaxy–galaxy lensing using maximum-likelihood lensing techniques is an example of such a method. Indeed, the goal of galaxy–galaxy lensing is to obtain constraints on the physical parameters that characterize the dark matter haloes of galaxies. This is accomplished directly using lensing because the deformation in the shapes of background galaxies produced by the foreground

*E-mail: marceau@ast.obs-mip.fr

lenses, although weak, is observationally detected statistically. The difficulty is that multiple deflections frequently occur along the line of sight, and therefore nearby groups or clusters can have an important effect yet again on the resultant distortions. This introduces a systematic bias in the mass obtained for the deflectors when using simple models.

Galaxy–galaxy lensing work began with the first detection of the signal from ground-based data (Brainerd, Blandford & Smail 1996, hereafter BBS) and later with the *Hubble Space Telescope* (*HST*) data (Griffiths et al. 1996). Maximum-likelihood techniques have been developed by Schneider & Rix (1997), Natarajan & Kneib (1997) and Geiger & Schneider (1998) to obtain constraints on galaxy halo properties in clusters and in the field. The results of these analyses suggest that galaxy haloes in clusters are significantly less massive but more compact compared to galaxy haloes around field galaxies of equivalent luminosity (Natarajan et al. 1998; Natarajan, Kneib & Smail 2002a). Besides, in the case of galaxy haloes in the field no clear edge is detected to the mass distribution even on scales of the order of a few hundred kpc (Fisher et al. 2000; McKay et al. 2001). Only two published studies to date by Hoekstra et al. (2003) and Hoekstra, Yee & Gladders (2004) have been able to put an upper bound on the characteristic extension of a field halo at about 290_{-82}^{+139} and $185_{-28}^{+30} h^{-1}$ kpc, which are only marginally consistent with each other. Besides, these large values do not impose a stringent constraint for typical galaxy mass distributions because at these typical radii the galaxy density is only a few times above the mean density of the Universe.

Galaxy–galaxy lensing studies provide information on average properties of the halo population; therefore, the results depend on the specific parametrized model chosen to fit the observational data. From a purely observational point of view, the reliability of the galaxy–galaxy lensing signal depends on the number density of galaxies whose distorted shapes can be reliably measured, as well as any additional constraints that can be added to the analysis, for instance, redshifts of the lens galaxies, redshifts of the source galaxies, galaxy type, dynamical constraints, and the presence of larger-scale structure such as groups or clusters in the vicinity.

Other methods to determine the masses of galaxies are generally based on the dynamical properties of the luminous matter: the measurement of the rotation curve or velocity dispersion; the study of the velocity field of nearby objects such as planetary nebulae, globular clusters and satellite galaxies. These dynamical methods are complementary to lensing, but often probe much smaller scales. The study of the velocity field around galaxies, for instance, is generally limited to local galaxies. However, with the large spectroscopic surveys such as the Two-Degree Field (2dF) and the Sloan Digital Sky Survey (SDSS), it is now possible to extend such analyses to larger scales (Brainerd & Specian 2003; Prada et al. 2003). Probing the dynamics of stars in galaxies is limited to the inner regions when studying high-redshift galaxies. Therefore, at the present time there is limited direct overlap between lensing and dynamical studies in terms of scales probed. However, this situation is likely to change in the very near future when large spectroscopic surveys of distant galaxies, such as the DEEP2 survey (Davis et al. 2003), the VIRMOS-VLT Deep Survey (VVDS; Le Fevre et al. 2003) or the z-COSMOS survey (<http://webast.ast.obs-mip.fr/zCosmos>), are completed.

The inner slopes of density profiles provide a strong test of structure formation in cold dark matter (CDM) models and lensing provides an unbiased way to estimate the slopes. Treu & Koopmans (2004) and Koopmans & Treu (2003) have studied the slope of the mass distribution at small radii (on scales ranging from a few to

about 20 kpc) by combining dynamical estimates and strong lensing constraints. They find that the mass distribution profile is flatter than the singular isothermal sphere (SIS) profile but steeper than the Navarro–Frenk–White (NFW) profile. Therefore, there is mounting evidence for the lack of cores (a constant density region) in galaxies as well as in clusters.

The galaxy–galaxy lensing results from the SDSS have also provided (McKay et al. 2001; Sheldon et al. 2003) interesting constraints on the distribution of light and dark matter in galaxies. Mass and light trace seem to trace each other reasonably well. The power of galaxy–galaxy lensing is that it provides a probe of the gravitational potential of the haloes of galaxies out to large radii, where no other methods are viable for intermediate-redshift as well as high-redshift galaxies, independent of the dynamical state of the system. A similar approach combining dynamical estimates of the central part of galaxies and galaxy–galaxy lensing is planned in the future as part of the GEMS and COSMOS projects.

This paper is organized as follows. In Section 2, we describe the method adopted to model galaxy lenses, source galaxies, the simulations performed to recover the input parameters of the lenses and the calculation of the aperture mass. In Section 3, we present the results for three different classes of lens models considered in this work. In Section 4, we explore the results of reparametrizing the models. Whenever necessary, our results are scaled to the currently preferred flat, low-matter density Λ CDM cosmology with $\Omega_M = 0.3$, $\Omega_\Lambda = 0.7$ and a Hubble constant $H_0 = 65 h_{65} \text{ km s}^{-1} \text{ Mpc}^{-1}$. In such a cosmology, at $z = 0.2$, 1 arcsec corresponds to $3.55 h_{65}^{-1}$ kpc.

2 GALAXY–GALAXY LENSING

We briefly review the basic principles of gravitational lensing of distant galaxies before describing the mass distributions adopted to model them. This section concludes with the presentation of our method to recover the lensing galaxy parameters.

2.1 Lensing equation

The light rays emitted by a distant galaxy are deflected en route to us by the presence of mass concentrations along the line of sight. The distortion can produce strong effects such as multiple images or arcs if there is close alignment between the distant source and a foreground source. However, most of the time only a weak distortion occurs in the galaxy shape.

Let us consider the multiple lensing equation (Schneider, Ehlers & Falco 1992). For two lenses A and B, the lens equation becomes

$$\beta = \theta - \alpha_A \frac{D_{AS}}{D_{OS}} - \alpha_B \frac{D_{BS}}{D_{OS}} \quad (1)$$

where β is the source position, α_A is the deflection due to the lens A, α_B is the deflection due to the lens B and D_{AS} , D_{BS} and D_{OS} are the angular diameter distances between source plane S and lens A, lens B and the observer, respectively (note that we must have $z_A < z_B < z_S$). The deflection angle α_X due to the lens X is proportional to the angular distance D_{OX} between observer and lens X and to the gradient of the projected gravitational potential ϕ generated by the lens X.

For a given background galaxy (i) and its associated lens (j), we can construct the amplification matrix a_{ij} , which provides the mapping between the source plane and the image plane

$$a_{ij} = \begin{pmatrix} 1 - \kappa^{ij} - \gamma_1^{ij} & -\gamma_2^{ij} \\ -\gamma_2^{ij} & 1 - \kappa^{ij} + \gamma_1^{ij} \end{pmatrix} \quad (2)$$

where κ is the convergence and γ_1 and γ_2 are the two components of the shear. In the case of multiple deflections (more than one lens contributing to the observed distortion), we will assume that the total amplification matrix a_i of the distant galaxy (i) is equal to the sum of the individual contributions a_{ij} from each lens:

$$a_i = \sum_j a_{ij}. \quad (3)$$

This assumption relies on the fact that we are in the weak lensing regime and that the distance between the lenses is large compared to the Einstein radius of each individual lens. For instance, in the simulations performed in this paper, the separation between two lenses is larger than 3 arcsec, when a typical value for the Einstein radius is about 1 arcsec.

2.2 Modelling the mass distribution of galaxies

Lensing probes the two-dimensional projected mass along the line of sight; therefore, we deal with the two-dimensional potential, $\phi(R)$, resulting from the three-dimensional density distribution $\rho(r)$ projected on to the lens plane. The related projected surface mass density Σ is then given by

$$4\pi G \Sigma(R) = \nabla^2 \phi(R). \quad (4)$$

Moreover, we are interested in the two-dimensional projected mass inside radius R (the aperture radius R_{aper}) defined as follows:

$$M_{\text{aper}}(R) = 2\pi \int_0^R \Sigma(r) r dr. \quad (5)$$

In this paper, we study three different mass models: (i) the two-component pseudo-isothermal mass distribution (PIEMD; Kneib et al. 1996), which is a more physically motivated mass profile than the isothermal sphere profile (SIS) but sharing the same profile slope at intermediate radius; (ii) the NFW (Navarro, Frenk & White 1997) profile; (iii) a power-law (PL) profile with core radius. These enable us to explore a wide range of mass distributions and to reveal the important parameters to which lensing is sensitive. The characteristic scales used to describe the different mass profiles are given in arcsec. We assume that the lenses have a circular geometry and are at a redshift of 0.2.

2.2.1 PIEMD profile

The density distribution for this model is given by

$$\rho(r) = \frac{\rho_0}{(1 + r^2/r_{\text{core}}^2)(1 + r^2/r_{\text{cut}}^2)} \quad (6)$$

with the core radius r_{core} of the order of 100 pc, and a truncation radius r_{cut} . We also introduce a shape parameter $a = r_{\text{cut}}/r_{\text{core}}$. In the centre, $\rho \simeq \rho_0/(1 + r^2/r_{\text{core}}^2)$, which describes a core with central density ρ_0 . The transition region ($r_{\text{core}} < r < r_{\text{cut}}$) is isothermal, with $\rho \simeq r^{-2}$. In the outer parts, the density falls off as $\rho \simeq r^{-4}$, as is usually required for models of elliptical galaxies. Fig. 1 illustrates this behaviour. These models have been successfully used by Natarajan et al. (1998, 2002a) to fit observed early-type galaxies in cluster lenses.

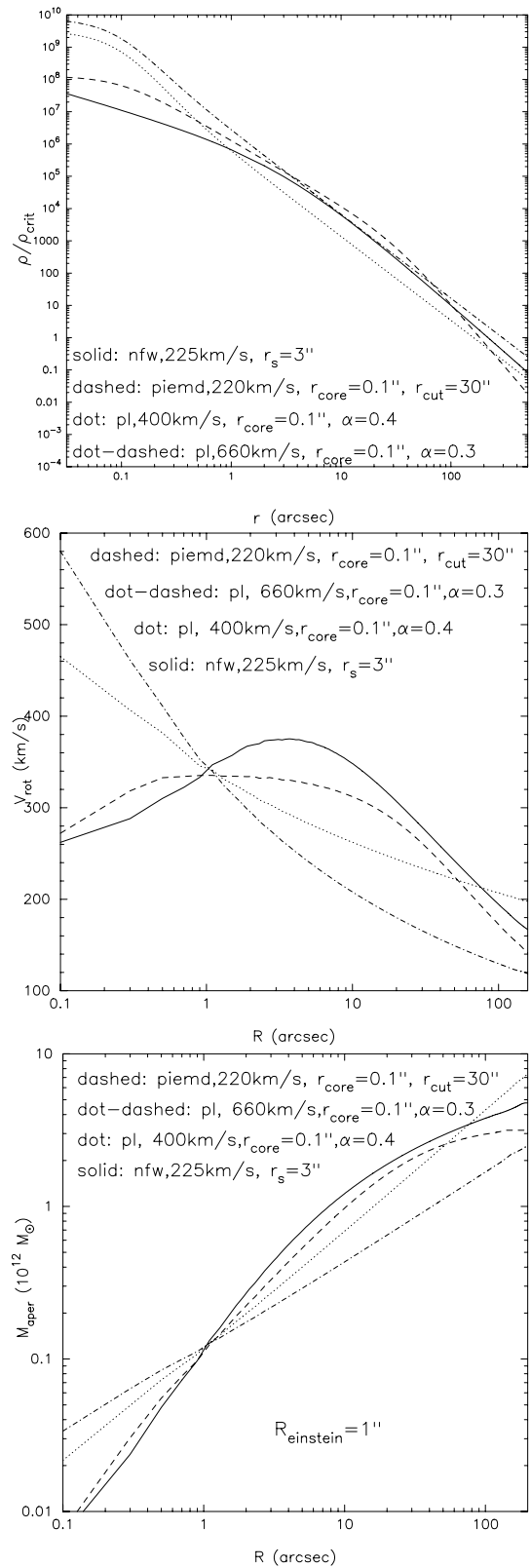


Figure 1. The density profile $\rho(r)$, the rotation velocity $V_{\text{rot}}(R)$ and the aperture mass $M_{\text{aper}}(R)$ for the three different mass profiles studied in this paper. For each of these model profiles, the relevant parameter choices are shown in the figure, for a circular lens at $z = 0.2$.

Integrating equation (6), we obtain the two-dimensional surface mass density distribution

$$\Sigma(R) = \frac{\sigma_0^2 r_{\text{cut}}}{2G(r_{\text{cut}} - r_{\text{core}})} \left(\frac{1}{\sqrt{r_{\text{core}}^2 + R^2}} - \frac{1}{\sqrt{r_{\text{cut}}^2 + R^2}} \right). \quad (7)$$

Here, σ_0 is the central velocity dispersion for a circular potential related to ρ_0 by the following relation:

$$\rho_0 = \frac{\sigma_0^2}{2\pi G} \left(\frac{r_{\text{cut}} + r_{\text{core}}}{r_{\text{core}}^2 r_{\text{cut}}} \right). \quad (8)$$

It can be shown that, for a vanishing core radius, the surface mass profile obtained above becomes identical to the surface mass profile used by BBS for modelling galaxy–galaxy lensing. The enclosed two-dimensional aperture mass interior to radius R is

$$M_{\text{aper}}(R) = \frac{\pi r_{\text{cut}} \sigma_0^2}{G} \left(1 - \frac{\sqrt{r_{\text{cut}}^2 + R^2} - \sqrt{r_{\text{core}}^2 + R^2}}{r_{\text{cut}} - r_{\text{core}}} \right). \quad (9)$$

The total mass of such a model is finite and is given by

$$M_{\text{tot}} = \frac{\pi \sigma_0^2}{G} \frac{r_{\text{cut}}^2}{r_{\text{cut}} + r_{\text{core}}} \simeq \frac{\pi \sigma_0^2 r_{\text{cut}}}{G}. \quad (10)$$

Fig. 1 shows the behaviour of M_{aper} as a function of the aperture radius R_{aper} and of $\rho(r)$ for such a profile, with $\sigma_0 = 220 \text{ km s}^{-1}$, $r_{\text{core}} = 0.1 \text{ arcsec}$, $r_{\text{cut}} = 30 \text{ arcsec}$. $\rho(r)$ is also shown, normalized to the critical density of the Universe ρ_{crit} , where $\rho_{\text{crit}} = 3H_0^2/8\pi G$.

2.2.2 NFW profile

The NFW density profile (Navarro et al. 1997) provides the best fit to the haloes that form in N -body simulations of collisionless dark matter. In fact, the NFW profile reproduces with good accuracy the radial distribution of structures in these simulations over nine orders of magnitude in mass (from the scale of globular clusters to that of massive galaxy clusters). Because it is thought that matter in the Universe is dominated by a form of dissipationless CDM, this ‘universal profile’ offers an interesting and natural way of describing mass concentrations. The density distribution of the NFW profile is given by

$$\rho(r) = \frac{\rho_s}{(r/r_s)(1 + r/r_s)^2} \quad (11)$$

where ρ_s is a characteristic density. It is possible to parametrize this model in terms of M_{200} , which is the mass contained in a radius r_{200} where the criterion $\bar{\rho} = 200\rho_{\text{crit}}$ holds, and δ_c the density contrast (or equivalently $c = r_{200}/r_s$, the concentration parameter). We have the following relations between the two parametrizations:

$$\begin{aligned} \rho_s &= \delta_c \rho_c, & M_{200} &= \frac{800}{3} \pi r_{200}^3 \rho_c, \\ \delta_c &= \frac{200}{3} \frac{c^3}{\ln(1+c) - (c/1+c)}. \end{aligned} \quad (12)$$

The properties of the projected quantities depend on the ratio r/r_s , so it is useful to introduce the dimensionless radial coordinate, $x = r/r_s = R/r_s$. Moreover, the velocity dispersion $\sigma(r)$ of this potential, computed with the Jeans equation assuming an isotropic velocity distribution, gives an unrealistic central velocity dispersion [$\sigma(0) = 0$]. In order to compare the NFW potential with other potentials used to model lenses, we define a characteristic velocity σ_s as follows:

$$\sigma_s^2 = \frac{4}{3} G r_s^2 \rho_s. \quad (13)$$

The surface mass density for the NFW is given by

$$\Sigma(x) = \int_{-\infty}^{+\infty} \rho(r_s, x, z) dz = 2\rho_s r_s F(x) \quad (14)$$

with

$$F(x) = \begin{cases} \frac{1}{x^2 - 1} \left(1 - \frac{1}{\sqrt{1-x^2}} \operatorname{argch} \frac{1}{x} \right) & (x < 1) \\ \frac{1}{3} & (x = 1) \\ \frac{1}{x^2 - 1} \left(1 - \frac{1}{\sqrt{x^2-1}} \arccos \frac{1}{x} \right) & (x > 1) \end{cases} \quad (15)$$

The two-dimensional aperture mass M_{aper} contained within the dimensionless radius x is (Bartelmann 1996)

$$M_{\text{aper}}(R) = \frac{3\pi \sigma_s^2 r_s}{2G} g(x) \quad (16)$$

with

$$g(x) = \begin{cases} \ln \frac{x}{2} + \frac{1}{\sqrt{1-x^2}} \operatorname{argch} \frac{1}{x} & (x < 1) \\ 1 + \ln \left(\frac{1}{2} \right) & (x = 1) \\ \ln \frac{x}{2} + \frac{1}{\sqrt{x^2-1}} \arccos \frac{1}{x} & (x > 1) \end{cases} \quad (17)$$

The mass M_{200} can be written as a function of σ_s , r_{200} and c :

$$M_{200} = 200\pi \frac{c^2}{\delta_c} \frac{\sigma_s^2 r_{200}}{G}. \quad (18)$$

Fig. 1 shows the behaviour of M_{aper} as a function of the aperture radius R_{aper} and of $\rho(r)$, with $\sigma_s = 225 \text{ km s}^{-1}$ and $r_s = 3 \text{ arcsec}$. This profile has a concentration parameter $c = r_{200}/r_s \simeq 12$, a typical value for a galaxy, and a projected mass inside r_{200} : M_{200} of $\sim 3 \times 10^{12} M_{\odot}$.

2.2.3 Power-law profile with a core

Another simple model to describe the mass distribution of a galaxy is a PL model with a core. In a CDM-dominated hierarchical structure formation scenario, mass profiles are expected to be independent of the mass scale, and therefore a PL profile is of interest. The PL mass distribution has three parameters: a core radius r_{core} of the order of a kpc for an average galaxy, a central velocity dispersion, σ_0 measured in km s^{-1} , and an exponent (α) which defines the gradient of the mass distribution. The three-dimensional density profile is (Kneib 1993)

$$\rho(r) = \rho_0 \frac{1 + (1 - 2\alpha/3)(r/r_{\text{core}})^2}{[1 + (r/r_{\text{core}})^2]^{2+\alpha}}. \quad (19)$$

Introducing $x = r/r_{\text{core}}$, the density profile falls off as $\rho \simeq x^{-2(1+\alpha)}$. Note that the case $\alpha = 0$ corresponds to an isothermal sphere with a core radius, and $\alpha > 0$ defines density profiles steeper than an isothermal sphere with a core radius. The relation between ρ_0 and σ_0 is given by

$$\rho_0 = \frac{\sigma_0^2}{r_{\text{core}}^2} \frac{9(1-2\alpha)}{4\pi G}. \quad (20)$$

The surface mass density is

$$\Sigma(x) = \Sigma_0 \frac{1 + (1 - 2\alpha/2)x^2}{(1 + x^2)^{3/2+\alpha}} \quad (21)$$

and the two-dimensional aperture mass contained within the dimensionless radius x is

$$M_{\text{aper}}(R) = \frac{3(1+2\alpha)\sigma_0^2 r_{\text{core}}}{G} \frac{x^2 + x^4}{(1+x^2)^{3/2+\alpha}} I_{1+\alpha} \quad (22)$$

with

$$I_{1+\alpha} = \int_0^\infty \frac{dx}{(1+x^2)^{1+\alpha}}. \quad (23)$$

Fig. 1 shows the behaviour of $\rho(r)$ and $M_{\text{aper}}(r)$ for such a profile, with $\sigma = 400 \text{ km s}^{-1}$ and $\alpha = 0.4$ (in this case, $I_{1.4} = 1.06$).

2.3 Comparing these profiles

Beginning with the Boltzmann equation to describe the behaviour of the CDM collisionless particles that constitute a galaxy halo, the Jeans equation for a spherical potential and for an isotropic velocity distribution ($\sigma \equiv \sigma_r$) is given by

$$\frac{1}{\rho} \frac{d(\sigma^2 \rho)}{dr} = -\frac{d\Phi}{dr} \quad (24)$$

where Φ is the three-dimensional potential. Considering the limit at $+\infty$, wherein $\sigma(r) \rightarrow 0$ and $\rho(r) \rightarrow 0$ to perform the integration, we have

$$\sigma^2(r) = -\frac{1}{\rho(r)} \int_r^{+\infty} \rho(r') \frac{d\Phi(r')}{dr'} dr'. \quad (25)$$

Solving this equation does not lead generally to a simple analytical expression for the velocity dispersion.

Hence, one usually uses the rotation velocity defined as

$$V_{\text{rot}}^2(R) = \frac{GM_{\text{aper}}(R)}{R}. \quad (26)$$

Fig. 1 shows the behaviour of $V_{\text{rot}}(R)$ for the three different mass profiles studied here.

It can be shown that for any spherically symmetric profile, the mass inside the Einstein radius R_E is proportional to R_E^2 , so that profiles for which R_E is constant can be compared. It is easy to show (e.g. Kneib 1993) that

$$M_{\text{aper}}(R_E) = \pi \Sigma_{\text{crit}} R_E^2. \quad (27)$$

Thus, we adjust the parameters of the different mass profiles in order to have the same Einstein radius, and therefore the same mass within the Einstein radius. The results are illustrated in Fig. 2; this plot allows us to rescale the velocity dispersions derived for each profile. We can immediately see from this plot that for $r > 4 \text{ arcsec}$, the shears computed from the three profiles are comparable. Note that in the case of the PL profile there is a strong dependence of the velocity dispersion on the value of the exponent α . For example, the PL profile with $\sigma_0 = 660 \text{ km s}^{-1}$ and an exponent of 0.3 induces the same shear as one with $\sigma_0 = 400 \text{ km s}^{-1}$ and an exponent of 0.4. Therefore, there is degeneracy between the value of σ_0 and α for the PL profile. In order to illustrate the behaviour of the PL profile, we include this latter profile in Figs 1 and 2.

3 SIMULATING GALAXY-GALAXY LENSING

3.1 Measurement of background galaxy shapes

We study in detail the lensing effects in two observational scenarios: (i) a ground-based survey using a wide field camera and (ii)

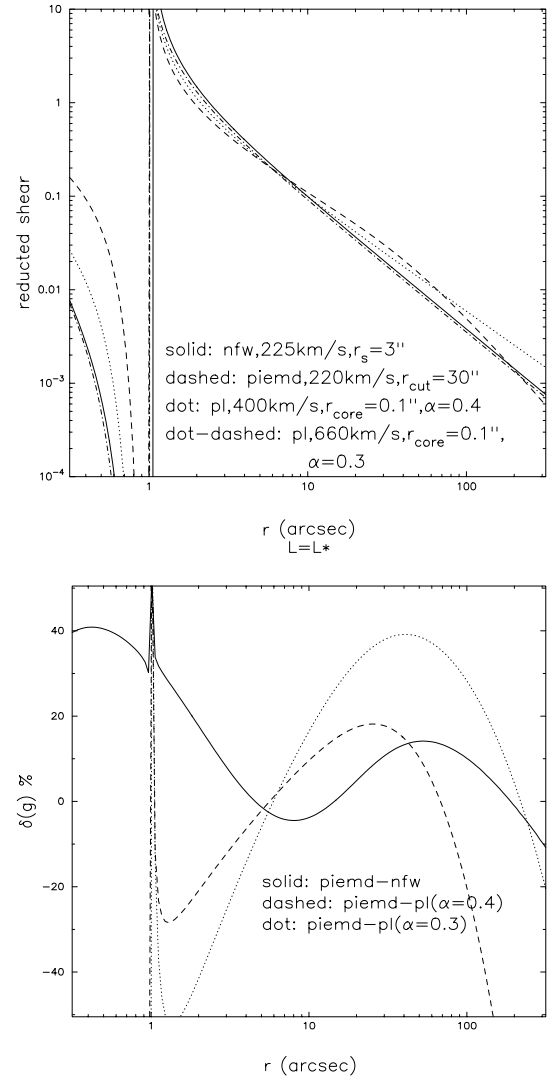


Figure 2. The reduced shears ($\gamma/1 - \kappa$) for the three different models for which the Einstein radius $R_E = 1 \text{ arcsec}$ (upper panel), and differences between them expressed as a percentage where we have used the PIEMD as the reference profile (lower panel).

data from space-based observations. Ground-based data are characterized by the following image quality: seeing of about 0.6–0.8 arcsec, and a galaxy number density of 20–40 galaxies per arcmin², of which only 50–70 per cent can generally be used to measure their shapes reliably. The above estimates were obtained from two hours of observation in the R band with the CFH12k camera with a field of view of $44 \times 28 \text{ arcmin}^2$.

Space observations have a significantly better image quality, with a point spread function of about 0.1–0.15 arcsec, and a galaxy number density of about 40–100 galaxies per arcmin² [*Super-Nova/Acceleration Probe (SNAP)* mission sensitivities; see Rhodes et al. 2004], of which about 80 per cent can be used in a weak lensing study because their shapes can be measured to the requisite degree of precision. Half an hour of observation in the R band of A2218 with the *HST* has provided the above estimates.

The measurement of shapes of lensed background galaxies is made using the second moment of the intensity of their light distribution. The quantity that is extracted for each galaxy is its complex ellipticity, e , defined as $e = e_1 + ie_2$. The magnitude of the

ellipticity is $e = \sqrt{e_1^2 + e_2^2}$, the mean ellipticity $m = (\sum_i e_i)/N$, and the dispersion of the ellipticity is equal to the square root of the variance, defined by $var = (\sum_i (e_i - m)^2)/N$, where N is the number of objects.

3.2 Scaling the mass distribution from the light distribution

The foreground lenses are described by a mass profile with known input parameters. The parameters used to describe the different lenses are scaled as a function of luminosity. The scaling relation for σ_0 assumes that mass traces light, and its origin resides in the Tully–Fisher or Faber–Jackson relations. The scaling relation for the radial parameter assumes that the mass-to-light ratio is constant for all galaxies. We do not take into account the scatter in these scaling relations. Note that there are other possible scaling relations, and that in principle we can test them with lensing.

3.2.1 PIEMD profile

We have for this profile

$$\sigma_0 = \sigma_0^* \left(\frac{L}{L^*} \right)^{1/4} \quad \text{and} \quad r_{\text{cut}} = r_{\text{cut}}^* \left(\frac{L}{L^*} \right)^{1/2}. \quad (28)$$

The parameter r_{core} is kept fixed at 0.1 arcsec, a fairly typical value for a galaxy.

From equation (13), we can scale the total mass with the luminosity as

$$M_{\text{tot}} = \frac{\pi \sigma_0^2 r_{\text{cut}}}{G} = \frac{\pi \sigma_0^{*2} r_{\text{cut}}^*}{G} \left(\frac{L}{L^*} \right)^{3/4}. \quad (29)$$

3.2.2 NFW profile

Similar to the PIEMD profile, we have

$$\sigma_0 = \sigma_0^* \left(\frac{L}{L^*} \right)^{1/4} \quad \text{and} \quad r_s = r_s^* \left(\frac{L}{L^*} \right)^{1/2}. \quad (30)$$

3.2.3 PL profile

For the PL profile, we have

$$\sigma_0 = \sigma_0^* \left(\frac{L}{L^*} \right)^{1/4} \quad \text{and} \quad r_{\text{core}} = r_{\text{core}}^* \left(\frac{L}{L^*} \right)^{1/2}. \quad (31)$$

In order to illustrate the coherence of these scaling laws, we show the shear profiles obtained for a typical faint ($L = L^*/10$) and bright ($L = 3L^*$) galaxy (see Fig. 3).

3.3 Background galaxies

The way we simulate the background source population is the same for the two cases when the lenses belong to a cluster versus when they are field galaxies, as follows.

(i) They are allocated random positions.

(ii) The number counts are generated in consonance with galaxy counts typical for a 2-h integration time in the R band. The magnitudes are assigned by drawing the number count observed with the Canada–France–Hawaii Telescope (CFHT).

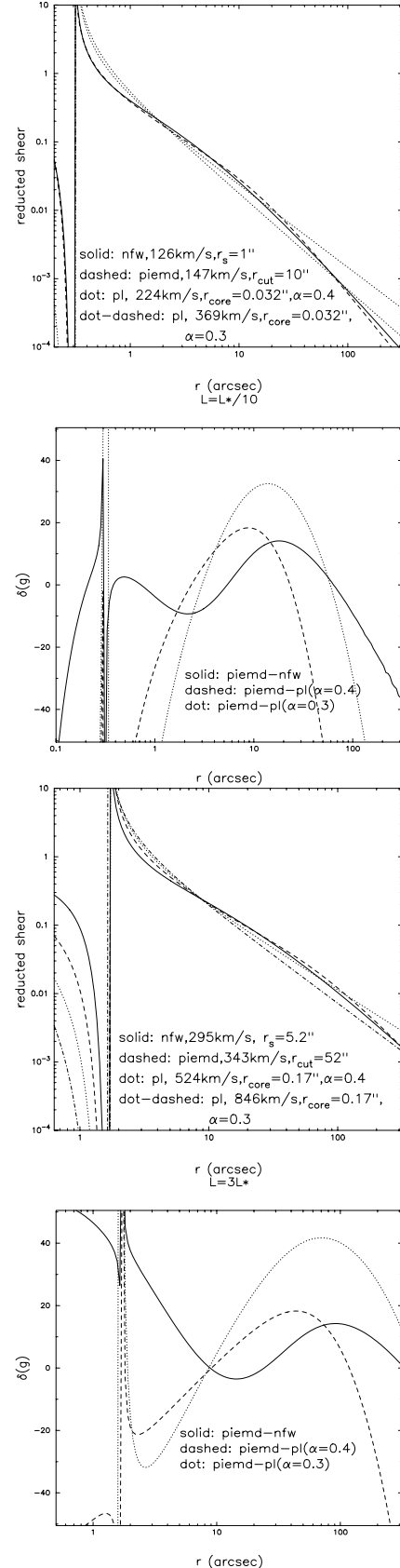


Figure 3. The reduced shears ($\gamma/(1 - \kappa)$) for each profile (panels 1 and 3) and differences between them expressed in percentages (panels 2 and 4), for $L = L^*/10$ and $L = 3L^*$ respectively, where once again the PIEMD is the reference profile.

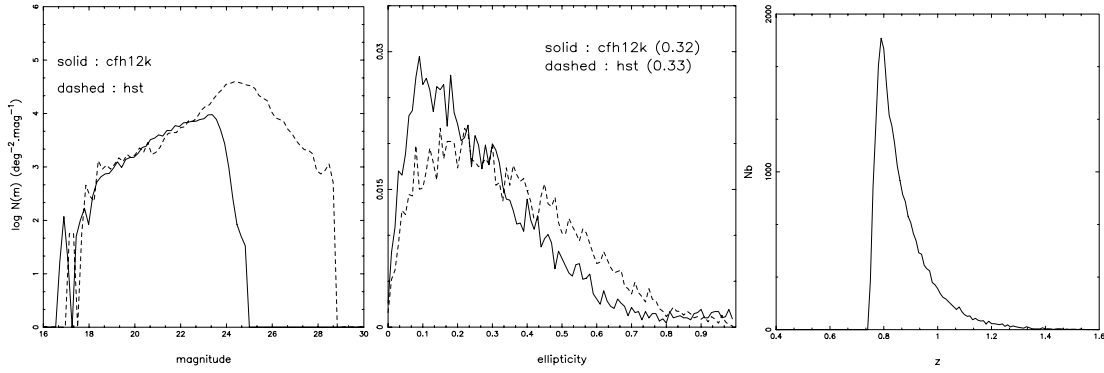


Figure 4. Galaxy counts from CFH12k and *HST* data (left panel), and the ellipticity distributions for the CFH12k and *HST* data (centre panel). The value in parentheses is the mean value of the ellipticity in each case. The right panel shows the redshift distribution of the background population in our simulations.

(iii) The shapes are assigned by drawing the ellipticity from a Gaussian distribution similar to the observed CFHT ellipticity distribution (see Fig. 4).

(iv) Redshift distribution. We use the *R* band to define the number counts of galaxies and use the *Hubble Deep Field* prescription in terms of the mean redshift per magnitude bin, and the same redshift distribution as BBS.

Note that from ground as well as from space, we use the same redshift distribution and do not take into account the effect of the geometry of the survey in these simulations. Moreover, the assumed redshift distribution shows a lack of any sources at redshift less than about 0.8. This is unrealistic, but the sources at $z < 0.8$ typically do not contribute significantly to the galaxy–galaxy lensing signal due to the functional form of the lensing efficiency. At low redshifts, intrinsic alignments of galaxies are also a contaminant but only at the few per cent level.

3.4 Lens galaxies

The way we simulate the foreground lenses galaxies is different in the case of galaxies inside the cluster and in the field. In both cases, the luminosity distribution is drawn from a luminosity function modelled on observational data.

3.4.1 Cluster galaxies

We put the individual lenses constituting a cluster at a redshift of 0.2, and model it as a superposition of large-scale smooth cluster component and a few clumps. In order to obtain a better match to the real data, the positions and the magnitudes of the foreground cluster galaxies are drawn from the positions and the magnitudes of ellipticals in the cluster A1689 at $z = 0.18$.

3.4.2 Field galaxies

For simplicity, the lenses are randomly distributed in position and uniformly distributed in a redshift range from 0.2 to 0.5. This distribution is a crude approximation of reality and we do not introduce any clustering of the lens galaxies.

4 MAXIMUM-LIKELIHOOD ANALYSIS

4.1 Methodology

Using the foreground cluster and field galaxies as the lens for the sheet of generated background galaxies, we use LENSTOOL to

solve the lensing equation and produce a catalogue of lensed background galaxies. This catalogue contains the following information for each lensed object: the position, the shape parameters and the redshift. Then this catalogue is processed through a numerical code that retrieves the input parameters of the lenses using a maximum-likelihood method as proposed by Schneider & Rix (1997) and as implemented by Natarajan & Kneib (1997). For each image (i), given a mass model for the foreground lensing galaxies, we can compute the amplification matrix a_i as a sum of the contribution from all the foreground galaxies j ; $z_j < z_i$ that lie within a circle of inner radius R_{\min} , and outer radius R_{\max} measured from the centre of the image (i):

$$a_i = \sum_{\substack{z_j < z_i \\ d(i,j) < R_{\max}}} a_{ij}. \quad (32)$$

The total shear experienced by a background galaxy γ_i can be obtained by summing the contributions from all the foreground galaxies j ; $z_j < z_i$ that lie within an annulus with inner and outer radii, respectively, at R_{\min} and R_{\max} .

Given the observed ellipticity ϵ_{obs}^i [defined as $\epsilon = (a - b)/(a + b)$] and the associated amplification matrix a_i , we are able to retrieve the intrinsic ellipticity ϵ_i^s of the source before lensing:

$$\epsilon_i^s = F(\epsilon_{\text{obs}}^i, a_i). \quad (33)$$

In the weak lensing regime, this relation can be simplified as

$$\epsilon_i^s = \epsilon_{\text{obs}}^i + \gamma_i. \quad (34)$$

In order to assign a likelihood to the parameters used to describe the lensing galaxies, we use P^s , the ellipticity probability distribution in the absence of lensing. Repeating this procedure for each image in the catalogue, we construct the likelihood function

$$\mathcal{L} = \prod_i P^s(\epsilon_i^s), \quad (35)$$

which is a function of the parameters used to define the mass models of the lenses. For each pair of chosen parameters, we can compute a likelihood function. The larger the likelihood function, the more accurate the retrieved parameters used to describe the lenses. The inversion from the observed ellipticity to the intrinsic ellipticity is fully analytical and takes into account all the non-linearities arising in the strong lensing regime, which may occur in the configuration with a cluster component.

The likelihood function for the parametric mass model for the lenses does have interesting convergence properties. The likelihood

surface is topologically complex because the degeneracies in the problem tend to produce several maxima. However, the convergence in both the cluster lens case and the field lens case is driven essentially by the width of the intrinsic ellipticity distribution of the sources. The degeneracies in this scheme are the generic ones that plague all lensing analyses: the mass sheet degeneracy (essentially the addition of a constant sheet of mass to the lens plane does not produce any discernible effect on the lensing of the background sources), the shot noise due to the finite number of sampled background sources and the details of the truncation of the mass profile of the lenses. The mass sheet degeneracy cannot be circumvented because we are necessarily measuring both the magnification κ and the shear γ from the same data points. Note that these are implicitly needed in computing the amplification matrix. Shot noise is more of a limitation in ground-based surveys when the number count of background galaxies is more sparse compared to the space-based data, despite the fact that lensing helps by magnifying fainter sources that normally would not make it into a magnitude-limited survey. The details of the mass profile and, in fact, the prescription used to truncate the mass at large radii influence the likelihood results. Because in galaxy–galaxy lensing (both in the field and interior to a cluster) we are most sensitive to the mass enclosed within an aperture and are less sensitive to the density profile in the inner regions, the truncation of the mass distribution at large radii drives the convergence of the likelihood function. This can be clearly seen in the plots where the influence of R_{\max} shows up directly in the likelihood contours (see Fig. 5). Note that the parameters chosen to characterize the mass model – the central velocity dispersion and the truncation radius – also contribute to the noise in the likelihood, thereby pointing to more efficient reparametrizations that we also explore in the final section of this paper.

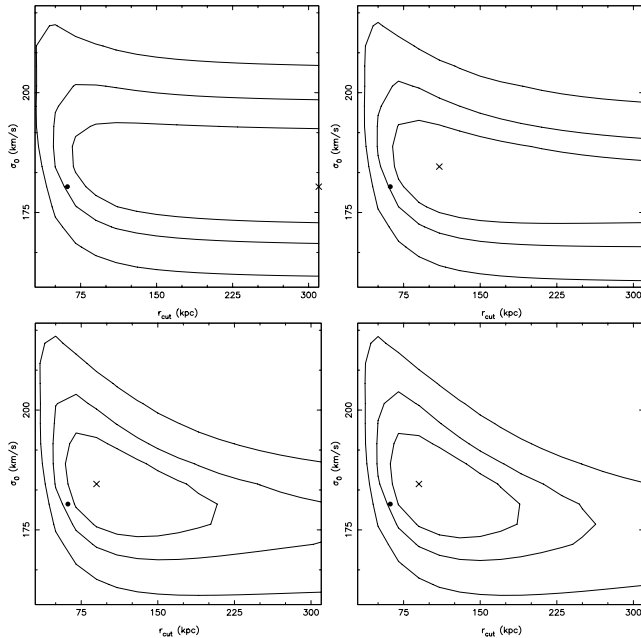


Figure 5. The PIEMD profile, in a field configuration. In the panels from left to right, the value of R_{\max} increases from 30, 60, 90 to 150 arcsec. When $R_{\max} > 100$ arcsec, the contours converge along the r_{cut} axis. Note that the convention throughout this paper is that the dot marks the value of the input parameters and the cross marks the retrieved output values.

4.2 Cluster weak lensing mass estimates

We construct a composite mass model for the cluster by superposing a large-scale smooth mass component and individual galaxies. As a first guess for the smooth mass model we use the averaged shear field obtained by simply binning up the shear in radial bins from the centre outward. This is a prior in the analysis that becomes modified with every iteration once the clumps are added to the model. We simulate the deformations induced by a clump with known parameters (which can be easily derived from a weak lensing analysis, for example). Then we add in the individual cluster galaxies and derive the shear of this composite system, which turns out to be larger than the shear for the clump alone as expected; this implies that we need to simultaneously modify the smooth component and the clumps during the optimization process. In massive lensing clusters, about 10 per cent of the total mass is associated with the individual galaxies (Natarajan et al. 2002a). This large-scale clump is described by a PIEMD profile with the following parameters: $\sigma_0 = 1070 \text{ km s}^{-1}$, $r_{\text{cut}} = 930 \text{ kpc}$ and $r_{\text{core}} = 60 \text{ kpc}$. This gives a total integrated mass of $7.3 \times 10^{14} M_{\odot}$. The mass we partition to galaxies is of the order of $7.3 \times 10^{13} M_{\odot}$. How do we modify the parameters of the large-scale clump in order to match the shear field? We find that the velocity dispersion of the large-scale clump needs to be reduced by about 5 per cent, keeping the others parameters fixed to accommodate the clumpiness.

5 RESULTS

We present the results obtained for the simulated data set, for the PIEMD, NFW and truncated PL models for two different configurations (Figs 6–8). The points mark the value of the input parameters used in order to generate the simulated catalogue, and the cross denotes the value of the output parameters as estimated from the maximum-likelihood analysis. We refer to the different plots by assigning them a number: the first is the upper-left plot, and the last (plot 9) is the lower-right plot. The first plot shows the reference field situation: 25 000 elliptical sources in a field of $26 \times 26 \text{ arcmin}^2$, which translates into a number density of about 35 galaxies per arcmin^2 . Then the following plots (2, 3 and 4) show the results obtained with 25 000 circular sources, then with 40 000 elliptical sources mimicking typical space observations with a density of 60 galaxies per arcmin^2 , then with 12 500 elliptical sources, corresponding to the ground-based configuration with a galaxy density of 17 per arcmin^2 , in a field configuration. Note that, in the case of circular sources, we do not have to deal with the intrinsic ellipticity noise; the detection is therefore improved and the contours are tighter. Plots 5 and 6 demonstrate the effect of the unknown redshift distribution for the background sources in a field configuration, when the redshift of the lenses is assumed to be known. The last row represents the cluster configuration: the ‘standard’ configuration (plot 7), then configurations where an uncertainty on the cluster has been introduced (plots 8 and 9). For each plot, the contours represent the 3σ , 4σ and 5σ confidence levels and, along the dotted lines, the mass within a projected radius $R_{\text{aper}} = 100 \text{ kpc}$ is constant, equal to the value indicated on the plot.

5.1 Number of background lenses

For each profile, in the field configuration, we explore the influence of the background density on the detection. The ‘standard’ configuration has 25 000 background sources (a density of 35 galaxies per

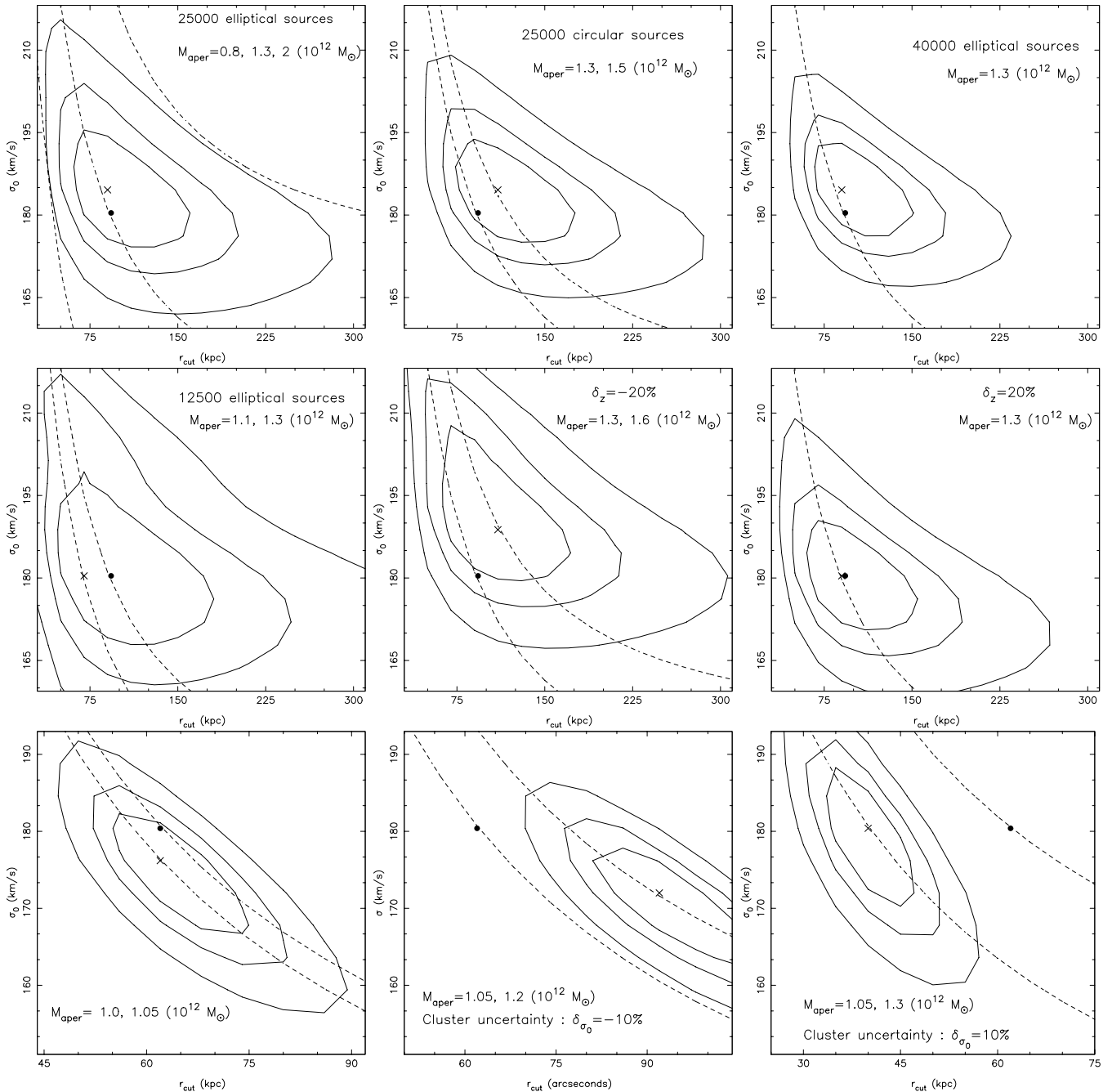


Figure 6. Results for the PIEMD profile. The top-left plot (plot 1) is the reference field situation with 25 000 elliptical background sources in a field of 26×26 arcmin², corresponding to a density of background sources equal to about 35 galaxies per arcmin². Then the following plots (2, 3 and 4) show the results obtained with 25 000 circular sources, then with 40 000 elliptical sources mimicking typical space observations with roughly 60 galaxies per arcmin², then with 12 500 elliptical sources, corresponding to the ground-based configuration with a galaxy number density of 17 galaxies per arcmin². Plots 5 and 6 show the effect of introducing an uncertainty in the mean redshift of the source population; this uncertainty is equal to -20 per cent (left) and $+20$ per cent (right), and no uncertainty is introduced for the lens redshift. The last row shows the results from the cluster configuration: the reference cluster configuration (plot 7), then configurations where an uncertainty on the cluster modelling is introduced, knowing the central velocity dispersion of the cluster to within ± 10 per cent. The contours in this figure represent the 3σ , 4σ and 5σ confidence levels, and along the dotted lines in every panel, the mass within a projected radius R_{aper} of 100 kpc is kept constant at the value indicated on the plot. Note that the dot indicates input values and the cross denotes the retrieved output.

arcmin²). We explore what happens when we increase this number to 40 000 (60 per arcmin²), or reduce it to 12 500 (17 per arcmin²). 17 galaxies per arcmin² corresponds to simulating ground-based survey data, whereas 60 galaxies per arcmin² corresponds to the space-based survey data. The main difference between the ground and space configurations is that from space the statistics are sig-

nificantly improved, and so the detection contours are significantly narrower.

5.2 Effect of assigning redshifts from an assumed distribution

To quantify the uncertainty arising from not knowing the redshifts for background sources, we performed the analysis after assigning

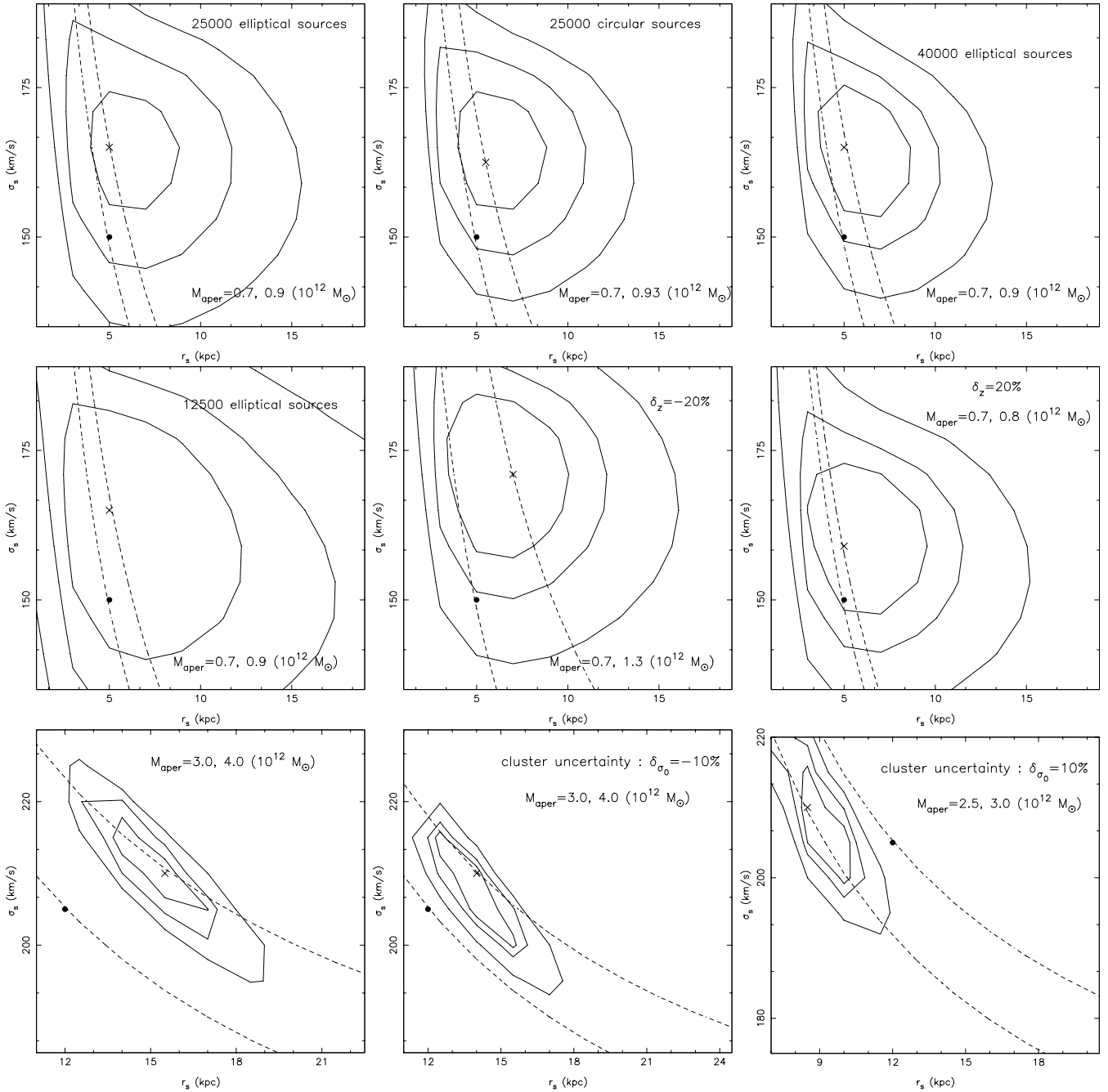


Figure 7. Results from the NFW profile. The top-left plot (plot 1) is the reference field situation with 25 000 elliptical background sources in a field of 26×26 arcmin², corresponding to a density of background sources equal to about 35 galaxies per arcmin². The following plots (2, 3 and 4) show the results obtained with 25 000 circular sources, then with 40 000 elliptical sources, corresponding to data obtained from space with 60 galaxies per arcmin², then with 12 500 elliptical sources, corresponding to the ground-based data of about 17 galaxies per arcmin². Plots 5 and 6 show the effect of introducing an uncertainty in the mean redshift of the source population; this uncertainty is equal to -20 per cent (left) and $+20$ per cent (right), and no uncertainty is introduced for the lens redshift. The last row shows the results from the cluster configuration: the reference cluster configuration (plot 7), the effect of introducing an uncertainty of ± 10 per cent in the central velocity dispersion of the cluster model used. Contours in these figures represent the 3σ , 4σ and 5σ confidence levels and, along the dotted lines in each panel, the mass within a projected radius R_{aper} of 100 kpc is kept constant, with M_{aper} at the quoted value indicated on the plot. Note that the dot indicates input values and the cross denotes the retrieved output.

redshifts drawn from a distribution. The 25 000 sources are put at a mean redshift z_s and images are simulated. When constructing the simulated catalogue, the background objects are assigned a mean redshift of $z_s + \delta_z$. This catalogue is then input into the maximum-likelihood code. Because the strength of the shear is proportional to

the distance between the sources and the lenses, underestimating the source redshifts leads to an overestimate of the lens masses and tends to shift the confidence contours toward higher values for the velocity dispersion. For the same reason, systematically overestimating the source redshifts leads to an underestimate of the galaxy masses. In

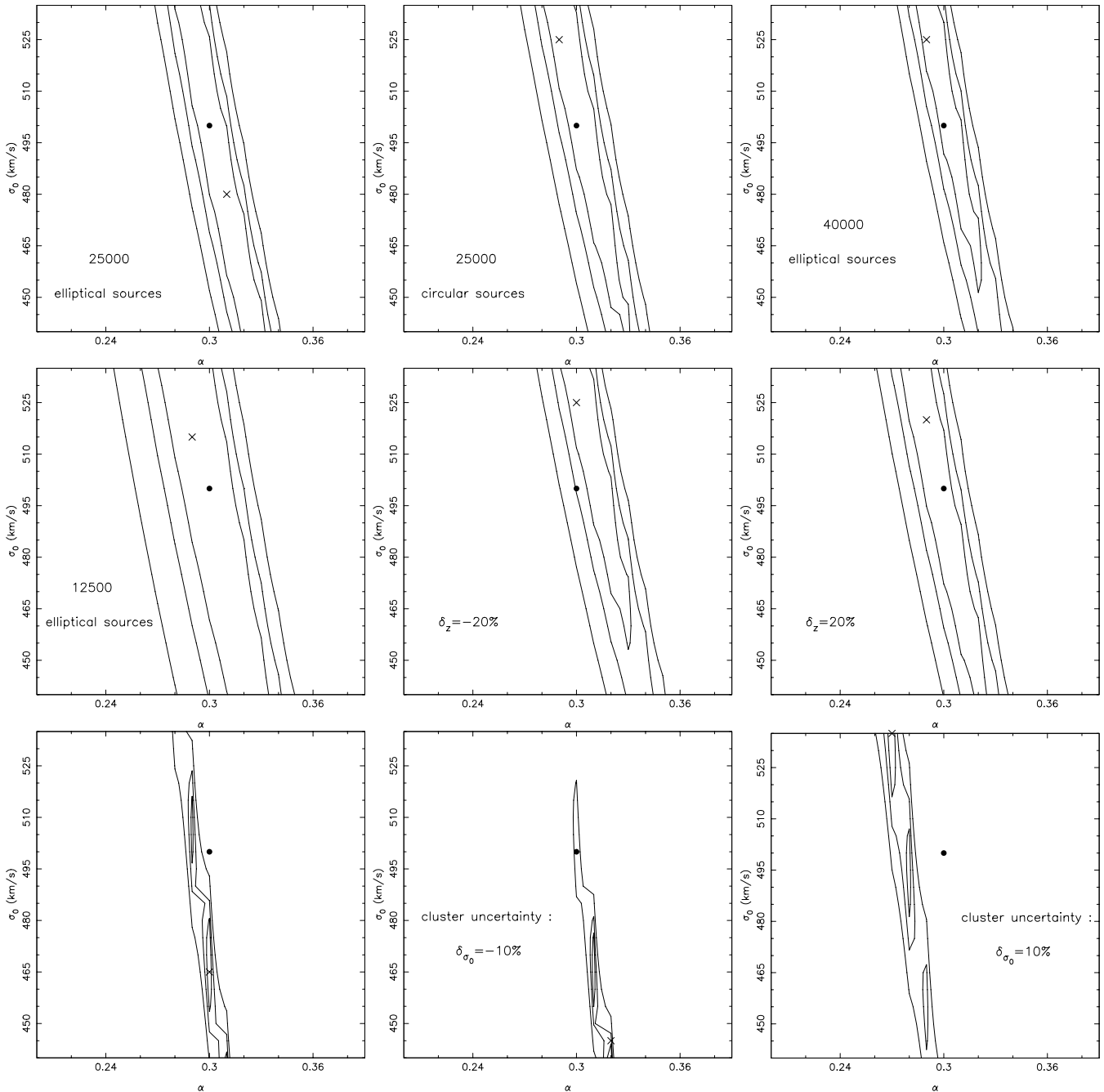


Figure 8. Results from the PL profile. The top-left plot (plot 1) is the reference field situation with 25 000 elliptical background sources in a field of 26×26 arcmin², corresponding to a density of background sources equal to about 35 galaxies per arcmin². Then the following plots (2, 3 and 4) show the results obtained with 25 000 circular sources, then with 40 000 elliptical sources corresponding to a typical space-based observation yielding 60 galaxies per arcmin², then with 12 500 elliptical sources corresponding to ground-based data with a galaxy number density of about 17 galaxies per arcmin². Plots 5 and 6 show the effect of introducing an uncertainty in the mean redshift of the source population; this uncertainty is equal to -20 per cent (left) and $+20$ per cent (right), and no uncertainty is introduced for the lens redshift. The last row shows the results from the cluster configuration: the reference cluster configuration (plot 7), and then configurations where uncertainty has been introduced in the cluster modelling. The contours in all these panels represent the 3σ , 4σ and 5σ confidence levels. Note that the dot indicates input values and the cross denotes the retrieved output.

any case, we find that a redshift uncertainty of ± 0.2 does not dramatically modify the conclusions. This is typically the precision we can obtain with photometric redshift estimation, which is encouraging for future surveys. These results are coherent with a recent study by Kleinheinrich et al. (2004) based on the galaxy–galaxy lensing results from the COMBO-17 survey. The 17 filters used in this sur-

vey provide a good estimation of a photometric redshift for both lens and source galaxies. This allows the authors to investigate how galaxy–galaxy lensing measurements are influenced by the knowledge of redshifts for lens and source galaxies. They found that it is of great importance to know the redshifts of individual lens galaxies in order to constrain the properties of their dark matter haloes,

Table 1. Influence of an uncertainty in the mean redshift of the sources. An error of δz_S corresponds to a variation of $E(z_L, z_S)$ equal to δE , which corresponds to a variation on σ_0 of the order of $\delta\sigma_0$. We see from this table that this estimated variation on σ_0 is coherent with the variation in the detection range as derived from the maximum-likelihood analysis.

δz_S (per cent)	δE	$\delta\sigma_0$	σ_0
0	0	0	[174–196]
20	0.05	–7	[170–190]
–20	–0.05	7	[180–208]

but that the knowledge of individual source redshifts improves the measurements only very little over use of statistical source redshift distribution. The sensitivity of the measurements on the lens redshift uncertainty is discussed by Kleinheinrich et al. (2004).

To be more quantitative, let us consider the lensing equation and express it for a constant deflection angle. For a PIEMD profile with a given σ_0 , we have

$$\sigma_0^2 \frac{D_{LS}}{D_S} = \text{constant} \quad \text{and} \quad \frac{D_{LS}}{D_S} = E(z_L, z_S) \quad (36)$$

as introduced in Golse (2002). Therefore, the equation can be rewritten as

$$\sigma_0^2 E(z_L, z_S) = \text{constant}. \quad (37)$$

The lenses are kept at a redshift of 0.2, and the mean redshift of the sources is changed by $\delta z = \pm 20$ per cent. We then evaluate the corresponding $\delta\sigma_0$ error introduced in the retrieval of the central velocity dispersion in the likelihood analysis; Table 1 gives the results. When we put an error of δz_S (per cent), this gives a variation of $E(z_L, z_S)$ equal to δE , and the corresponding variation on σ_0 is of the order of $\delta\sigma_0$. This range of values is given by the projection of the 3σ contours along the σ_0 axis. We can see that the variation in the detection range is in agreement with the calculations made.

5.3 Influence of the uncertainty in the cluster modelling

When working with the real data, we will have to put in by hand the description of the cluster. The reliability of the results will depend on the accuracy with which we describe the cluster. In order to study the influence of the uncertainty of the cluster profile, the cluster component is described by a PIEMD profile with a velocity dispersion of $\sigma_{\text{cluster}} = 1000 \text{ km s}^{-1}$. When constructing the simulated catalogue, the cluster component is assigned a velocity dispersion of $\sigma_{\text{cluster}} + \delta\sigma$. The likelihood is then computed for this case.

6 DISCUSSION AND CONCLUSIONS

6.1 Constraints obtained on mass profiles

For the PIEMD and NFW profiles, we have found that we are able to retrieve the characteristic halo parameters with a reasonable precision, for every configuration. In fact, interestingly enough, the dotted lines in Figs 6 and 7 show us that the aperture mass is retrieved very accurately. This immediately suggests the reparametrization of models considered here: rather than fitting in the (σ_0, r) plane, we can fit the deformations directly in the $(M_{\text{aper}}, R_{\text{aper}})$ plane. This formulation is explored in the next section.

For the PL profile, we find that we can put some constraints on α , the slope of the density profile, but not on the velocity dispersion, because the likelihood function does not always converge along that direction. So we can use this profile to estimate the slope of

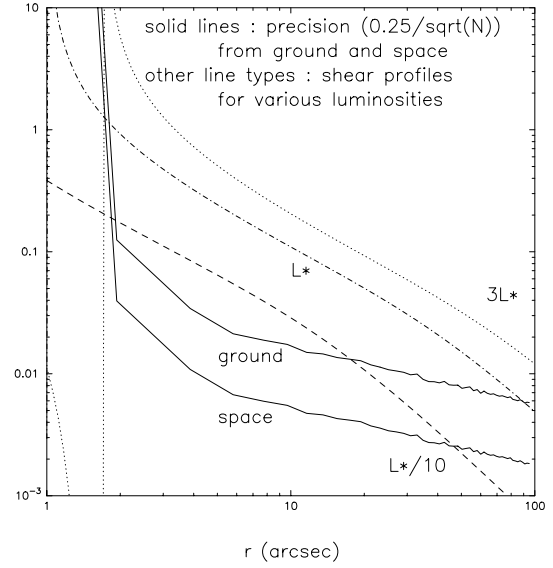


Figure 9. Comparing the signal-to-noise for an estimate of the optimal choice for R_{max} . The solid lines correspond to the characteristic ellipticity (due to the width of the ellipticity distribution), $0.25/\sqrt{N}$ as a function of radius, from ground and space. The other line types (dot, dashed and dot-dashed) correspond to the signal – the reduced shear as a function of radius for typical luminosities.

dark matter haloes, without trusting the constraints we obtain on the velocity dispersion for the profile.

6.2 Influence of R_{max}

When working with real data, the results we obtain depend on the value chosen for R_{max} . When we take a low value for R_{max} , the shear for the image (i) is calculated with fewer lenses, and we find that the contours do not close in r_{cut} . When the value of this parameter is increased, the contours converge and close. On the other hand, picking a high value for R_{max} introduces some noise in calculating the shear, and can dilute the galaxy–galaxy lensing signal significantly: lenses that do not effectively participate in the lensing of an image if utilized in the calculation become a source of noise. Fig. 5 illustrates precisely this situation: for a given value of R_{max} , we obtain a good estimate of σ_0 , but the robustness of the constraint on r_{cut} is directly related to the value of R_{max} . Others authors have reported that their results are sensitive to the value of this parameter (e.g. Kleinheinrich 2003).

The choice of R_{max} is therefore important. To obtain the order of magnitude of this parameter, we compare the characteristic noise in the problem, i.e. $0.25/\sqrt{N}$, to the signal we are sensitive to, i.e. the reduced shear; the factor of 0.25 is the width of the intrinsic ellipticity distribution and N is the number of background objects at a distance r from a lensing galaxy. This noise has been estimated by analysing data from the ground-based CFH12k observations of the cluster A1763 at a redshift of $z = 0.22$. From space, we expect the number of background objects to be about six/seven times higher. Fig. 9 shows that a value of about 100 arcsec can be used for R_{max} . On the other hand, the choice of the parameter R_{min} does not influence the results, so we fix this parameter to be of the order of a few kpc.

7 REPARAMETRIZATION OF THE PROBLEM

Thus far, we have performed the likelihood analysis to optimize the values of two parameters σ_0 and r_{cut} (or r_s). A different set of

parameters can be chosen for maximizing the likelihood, for instance M_{aper} and R_{aper} , which we explore below.

We have

$$\mathcal{L} = \mathcal{L}(\sigma_0, r_{\text{cut}}) \quad \text{and} \quad M_{\text{aper}} = M_{\text{aper}}(R_{\text{aper}}, \sigma_0, r_{\text{cut}}) \quad (38)$$

so we can write

$$\sigma_0 = \sigma_0(M_{\text{aper}}, R_{\text{aper}}, r_{\text{cut}}). \quad (39)$$

The likelihood function then becomes

$$\mathcal{L}(M_{\text{aper}}, R_{\text{aper}}, r_{\text{cut}}) \quad (40)$$

and by summing over r_{cut} , we obtain

$$\mathcal{L}' = \sum_{r_{\text{cut}}} \mathcal{L}(M_{\text{aper}}, R_{\text{aper}}, r_{\text{cut}}) \quad (41)$$

$$\mathcal{L}' = \mathcal{L}'(M_{\text{aper}}, R_{\text{aper}}). \quad (42)$$

The sum is performed for a set of r_{cut} values around the input value used to simulate the catalogue and the range defined by the projection of the 3σ contour level along the r_{cut} axis. The results do not depend strongly on the range used to do the sum. Figs 10 and 11 show the \mathcal{L}' contours we obtain for the NFW and PIEMD

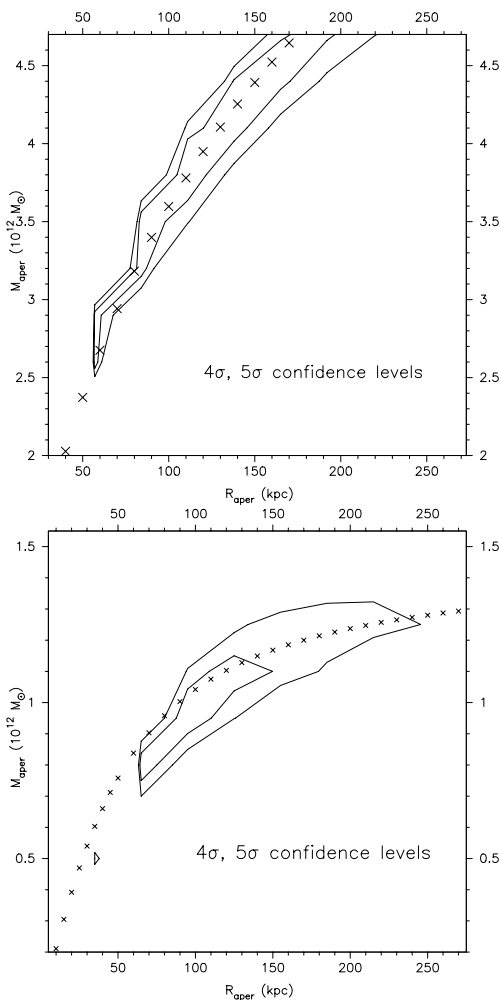


Figure 10. The likelihood $\mathcal{L}'(M_{\text{aper}}, R_{\text{aper}})$ for the NFW (upper panel) and PIEMD (lower panel) profiles. The crossed line represents the $M_{\text{aper}}(R_{\text{aper}})$ contour obtained with the input parameters used to describe the foreground lenses in the cluster configuration.

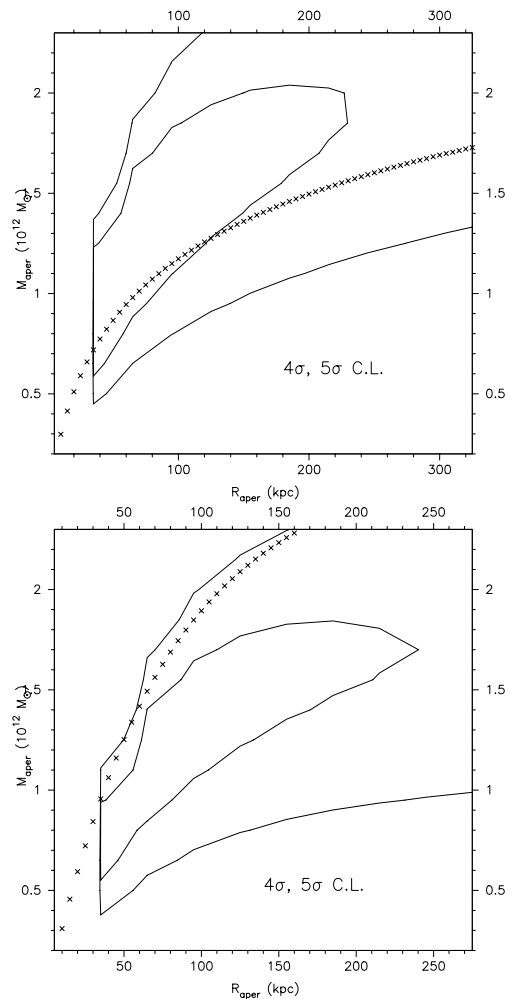


Figure 11. The likelihood $\mathcal{L}'(M_{\text{aper}}, R_{\text{aper}})$ for the NFW (upper panel) and PIEMD (lower panel) profiles. The crossed line represents the $M_{\text{aper}}(R_{\text{aper}})$ contour obtained with the input parameters used to describe the foreground lenses in the field configuration.

profiles. Because the PL profile does not have a cut-off radius, we cannot compare it easily with the reparametrized PIEMD and NFW profiles. The plots above show that we can put strong constraints on the aperture mass; the crossed line represents the line $M_{\text{aper}}(R_{\text{aper}})$ as computed with the input model used to generate the simulated catalogue.

The motivation of such a reparametrization is that we deal with more direct physical quantities than halo parameters, i.e. an aperture mass calculated within an aperture radius. The primary motivation for galaxy–galaxy lensing studies was to measure halo masses, so this offers a more convenient parametrization for this purpose. This is also a different way of measuring masses compared to the aperture densitometry method. Moreover, it is more suited to the case of clustered galaxies because we are not able to integrate the shear profile for any individual galaxy.

To conclude in this paper, we have discussed galaxy–galaxy lensing in the context of measuring masses of field and cluster galaxies. We compare the robustness of recovering input parameters for the mass distribution of lenses from a ground-based survey and space-based observations. We explore a wide range of input mass models for galaxy haloes. We simulate the galaxy–galaxy lensing effect and generate synthetic catalogues. A maximum-likelihood

method is applied to the catalogues to successfully recover the lens parameters in various configurations. Going beyond the standard parametrization of a dark matter halo, we propose a reparametrization of the problem in terms of more direct physical quantities: the aperture mass calculated within an aperture radius. The main result of this reparametrization is that we are able to put even stronger constraints on the aperture mass for an L^* galaxy.

ACKNOWLEDGMENTS

ML thanks the Astrophysics Department of the Pontificia Universidad Católica, Santiago, Chile for their hospitality, where a significant portion of this work was completed.

REFERENCES

- Bartelmann M., 1996, *A&A*, 313, 697
 Brainerd T. G., Specian M. A., 2003, *ApJ*, 593, L7
 Brainerd T. G., Blandford R., Smail I., 1996, *ApJ*, 466, 623 (BBS)
 Davis M. et al., 2003, in Guhathakurta P., ed., *Proc. SPIE 4834, Discoveries and Research Prospects from 6- to 10-Meter Telescopes II*. SPIE, Bellingham WA, p. 161
 Fassnacht C. D. et al., 1999, *AJ*, 117, 658
 Fischer P. et al., 2000, *AJ*, 120, 1198
 Gavazzi R., Fort B., Mellier Y., Pellò R., Dantel-Fort M., 2003, *A&A*, 403, 11
 Geiger B., Schneider P., 1998, *MNRAS*, 295, 497
 Golse G., 2002, PhD thesis, Université Paul Sabatier
 Griffiths R. E., Casertano S., Im M., Ratnatunga K. U., 1996, *MNRAS*, 282, 1159
 Hoekstra H., Franx M., Kuijken K., Carlberg R. G., Yee H. K. C., 2003, *MNRAS*, 340, 609
 Hoekstra H., Yee H. K. C., Gladders M., 2004, *ApJ*, 606, 67
 Keeton C. R., Kochanek C. S., Seljak U., 1997, *ApJ*, 482, 604
 Kleinheinrich M., 2003, PhD thesis, Max-Planck-Institut für Astronomie
 Kleinheinrich M. et al. 2004, *A&A*, submitted (astro-ph/0404527)
 Kneib J.-P., 1993, PhD thesis, Université Paul Sabatier
 Kneib J.-P., Ellis R. S., Smail I., Couch W. J., Sharples R. M., 1996, *ApJ*, 471, 643
 Kneib J., Cohen J. G., Hjorth J., 2000, *ApJ*, 544, L35
 Kneib J.-P. et al., 2003, *ApJ*, 598, 804
 Koopmans L. V. E., Treu T., 2003, *ApJ*, 583, 606
 Le Fevre O. et al., 2003, *Proc. SPIE*, 4834, 173
 McKay T. A. et al., 2001, *ApJ*, submitted (astro-ph/0108013)
 Möller O., Natarajan P., Kneib J.-P., Blain A. W., 2002, *ApJ*, 573, 562
 Natarajan P., Kneib J.-P., 1997, *MNRAS*, 287, 833
 Natarajan P., Kneib J.-P., Smail I., Ellis R., 1998, *ApJ*, 499, 600
 Natarajan P., Kneib J.-P., Smail I., 2002a, *ApJ*, 580, L11
 Navarro J., Frenk C. S., White S. D. M., 1997, *ApJ*, 462, 563
 Prada F. et al., 2003, *ApJ*, 598, 260
 Phillips P. M. et al., 2000, *MNRAS*, 319, L7
 Refregier A., 2003, *ARA&A*, 41, 645
 Rhodes J. et al. (*SNAP* Collaboration), 2004, *Astropart. Phys.*, 20, 377
 Schneider P., Rix H. W., 1997, *ApJ*, 474, 25
 Schneider P., Ehlers J., Falco E. E., 1992, *Gravitationnal Lenses*. Springer, New York
 Sheldon E. S., Frieman J., Johnston D., McKay T. (*SDSS* Collaboration), 2003, *Am. Astron. Soc. Meeting*, 202, 51.05
 Treu T., Koopmans L. V. E., 2004, *ApJ*, 611, 739

This paper has been typeset from a $\text{\TeX}/\text{\LaTeX}$ file prepared by the author.